

A Compact, Flexible, and Robust Micropulsed Doppler Lidar

PAUL SCHROEDER^a

Research Associateship Program, National Research Council, and Chemical Sciences Division, National Oceanic and Atmospheric Administration, Boulder, Colorado

W. ALAN BREWER

Chemical Sciences Division, National Oceanic and Atmospheric Administration, Boulder, Colorado

ADITYA CHOUKULKAR^b

Vibrant Clean Energy LLC, Boulder, Colorado

ANN WEICKMANN, MICHAEL ZUCKER, AND MAXWELL W. HOLLOWAY

Chemical Sciences Division, National Oceanic and Atmospheric Administration, and Cooperative Institute for Research in Environmental Sciences, Boulder, Colorado

SCOTT SANDBERG

Chemical Sciences Division, National Oceanic and Atmospheric Administration, Boulder, Colorado


(Manuscript received 26 August 2019, in final form 1 June 2020)

ABSTRACT

This work details a master oscillator power amplifier (MOPA) microjoule-class pulsed coherent Doppler lidar system configuration designed to measure line-of-sight wind velocities and backscatter intensity of atmospheric aerosols. The instrument is unique in its form factor. It consists of two physically separated modules connected by a 10 m umbilical cable. One module hosts the transceiver, which is composed of the telescope, transmit/receive (T/R) switch, and high-gain optical amplifier, and is housed in a small box (34.3 cm × 34.3 cm × 17.8 cm). The second module contains the data acquisition system and several electro-optical components. This form factor enables deployments on platforms that are otherwise inaccessible by commercial and research instruments of similar design. In this work, optical, electrical, and data acquisition components and configurations of the lidar are detailed and two example deployments are presented. The first deployment describes measurements of a controlled wildfire burn from a small aircraft to measure vertical plume dynamics and fire inflow conditions during summer in Florida. The second presents measurements of the marine boundary layer height and vertical velocity and variance profiles from the Research Vessel (R/V) *Thomas Thompson*. The new instrument has enabled greater flexibility in field campaigns where previous instruments would have been too costly or space prohibitive to deploy.

1. Introduction

Atmospheric phenomena like terrestrial and oceanic atmospheric boundary layer mixing processes (Garratt 1994; Tucker et al. 2009; Intrieri et al. 1989; Jia et al. 2019), low-level jets (Banta et al. 2002; Stensrud 1996), and atmospheric chemical transport (Lareau and Clements 2015; Strawbridge and Snyder 2004; Senff et al. 2010; Wang et al. 2019a) require real-world study and are important for climate/weather

 Denotes content that is immediately available upon publication as open access.

^a ORCID: 0000-0003-3368-953X.

^b ORCID: 0000-0003-1007-0267.

Corresponding author: W. Alan Brewer, alan.brewer@noaa.gov

DOI: 10.1175/JTECH-D-19-0142.1

© 2020 American Meteorological Society. For information regarding reuse of this content and general copyright information, consult the [AMS Copyright Policy \(www.ametsoc.org/PUBSReuseLicenses\)](https://www.ametsoc.org/PUBSReuseLicenses).

model validation. However, the few-meter to few-kilometer spatial scale of these features are unique to specific regions or terrain types on Earth's surface and need to be measured in situ. Fieldable and robust instruments are required that can probe these phenomena with different scanning scenarios to provide accurate, time-resolved estimates of the three-dimensional wind field (u, v, w) . A pulsed Doppler lidar is a laser-based remote instrument that meets these specifications.

Doppler lidars have been prevalent in atmospheric remote sensing for many years (Brewer and Hardesty 1995; Bilbro et al. 1984; Hall et al. 1984; Lawrence et al. 1972; Henderson et al. 1993). The first Doppler lidar developed at NOAA's Earth Systems Research Laboratory (ESRL) was a 10 μm , high-power system capable of interrogating up to 30 km and primarily designed for large-scale atmospheric transport measurements and horizontal scanning (Post et al. 1982). This system was physically large, expensive, and only transportable via a shipping container so was limited in field use to ships, large aircraft (Rothermel et al. 1998), or stationary ground deployments (Banta et al. 1992). Subsequent lidars from NOAA focused on shorter wavelength and smaller range, though with increased time- and spatial-resolution capability within the boundary layer (Brewer and Hardesty 1995; Grund et al. 2001). The high-resolution Doppler lidar (HRDL) (Grund et al. 2001) was a compact instrument that flew on small aircraft like the DLR Falcon (Kiemle et al. 2007; Tollerud et al. 2008) but could only be motion stabilized on large, slowly varying platforms like ships (Langley DeWitt et al. 2013). Modern Doppler lidar systems have exploited developments in fiber optics to address a need for compact and accurate instruments that are more easily deployed and cost effective. Though there are commercial systems available (Pearson et al. 2009; Wächter et al. 2008), many groups are still conducting research on these systems to minimize their volume, maximize their sensitivity, and increase resolved range (Xia et al. 2017; Yan et al. 2017; Abari et al. 2014; Wang et al. 2017, 2019b). This paper will address a recent push to advance lidar measurements by developing a compact, near-infrared, pulsed Doppler lidar built almost entirely with robust, telecommunications grade equipment that allows rapid and motion stabilized field deployments.

The system outlined in this work is the second version of a microjoule-class pulsed Doppler (MD2) lidar developed in the Atmospheric Remote Sensing group at ESRL. The first version, Micro Doppler 1, was a proof of concept for the fiber-based design and is housed in a 0.68 m³ cabinet. MD2 follows a master oscillator power amplifier (MOPA) configuration that has been designed

to allow deployment on mobile, cost effective platforms like small aircraft and passenger pickup trucks while foregoing the need for shipment and operation from a shipping container. It has up to a 7.2 km range and many important operating parameters are user configurable in the field. This article will discuss the following topics relevant to MD2: section 2—a detailed description of the instrument hardware, data processing techniques, and some of its operating parameters; section 3a—example data from a recent field campaign where data were collected with this system from the camera bay of a NOAA Twin Otter aircraft measuring horizontal and vertical winds over a controlled wildland fire burn; section 3b—measurements of vertical velocities and velocity variances measured from a ship-based measurement campaign on the Research Vessel (R/V) *Thomas Thompson*.

2. Instrument description

a. Optical fiber components

MD2 is constructed entirely with fiber components except for free-space optics as noted in Fig. 1 in the telescope and transmit/receive (T/R) switch. The lidar follows a MOPA design (Brewer and Hardesty 1995) with all fibers in the system being 1550 nm, 9 μm core, ferrule connector/angled physical contact (FC/APC) connectorized, and polarization maintaining (PM) unless otherwise noted. FC/APC connectors are used to maintain high transmission and reduce possible reflections within the fiber. The lidar pulse is formed from the output of a continuous wave master oscillator (MO; TeraXion PureSpectrum-NLL) that supplies the system with 80 mW of power at 1543.00 nm with a linewidth of <5 kHz. The laser output is coupled to a 95%/5% fiber splitter, where 5% is sent to a manual attenuator, followed by a 50%/50% mixer for later combination with the backscattered light and subsequent heterodyne detection. The 95% leg of the splitter is sent to an acousto-optic modulator (AOM; IntraAction E621NAA) operating at an intermediate frequency (IF) of 62.0 MHz and creates pulses at a rate of 15–20 kHz whose width and shape can be tuned with an arbitrary waveform generator (NI PXI-5412). The arbitrary waveform generator allows the input pulse width to be tuned as needed, generally between 166 and 1000 ns, and the input pulse shape to be adjusted to compensate for the time-dependent gain profile of the amplifier. The pulse shape is tuned for each pulse width until the launched pulse leaving the power amplifier is roughly Gaussian. The full width at half maximum (FWHM) pulse width directly corresponds to the desired range resolution of the lidar, as discussed later. The isolation of the AOM in its “off” state is 70.9 dB, which is made

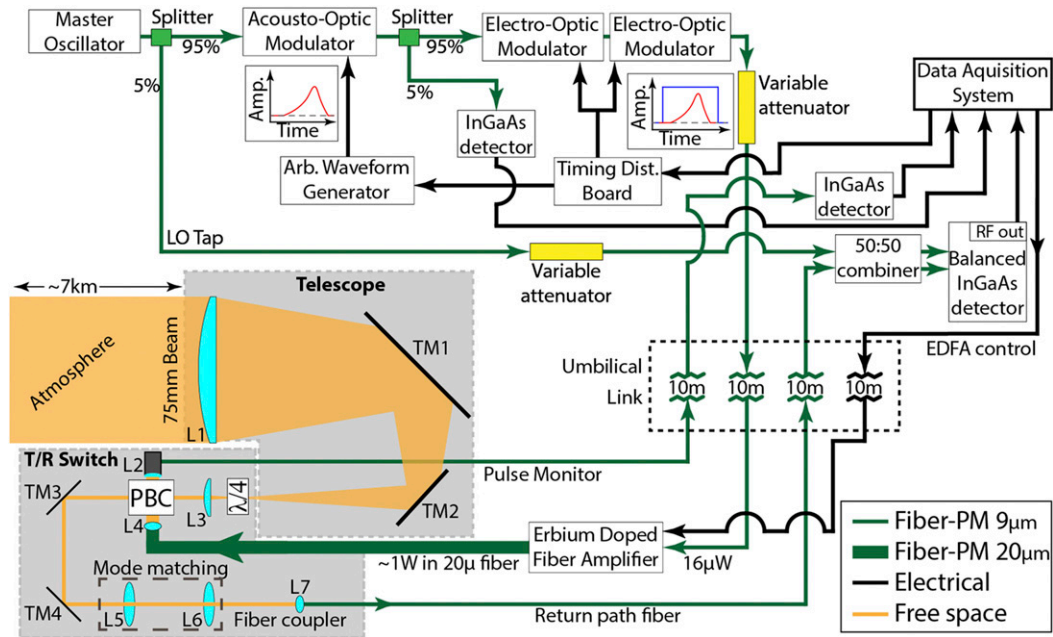


FIG. 1. Schematic of all electro-optical and free-space components for MD2. PM: polarization maintaining; LO: local oscillator; EDFA: erbium doped fiber amplifier; L1: 75-mm-diameter \times 500-mm-focal-length lens; TM1: 50 mm broadband mirror; TM2: same as TM1; T/R switch: transmit/receive switch; $\lambda/4$: quarter wave plate; L2: 12.5-mm-diameter transfer lens set; L3: 25-mm-diameter \times 30-mm-focal-length lens; PBC: polarizing beam cube; L4: fiber collimator (Thorlabs PAF-X-18-C); TM3: broadband mirror; TM4: same as TM3; L5: 25-mm-diameter \times 40-mm-focal-length lens; L6: 25-mm-diameter \times 50-mm-focal-length lens; L7: fiber collimator (Thorlabs PAF-X-11-C).

possible by a custom radio frequency (RF) driver architecture that removes the RF source prior to amplification between pulses. The custom AOM driver was required to increase optical isolation thus minimizing amplification of continuous wave (CW) leak through and amplified spontaneous emission (ASE) light by the erbium doped fiber amplifier (EDFA; Keopsys PEFA-LP-C-PM-E04-1543-ET1-PE2D-FA-FA). Back reflections of this spurious CW output off the transmit optics can saturate the detector and dominate the weak, backscattered light during measurement of atmospheric return. Following the pulse creation through the AOM, the light is again split with a 95%/5% splitter, where the 5% line goes to a detector (Thorlabs DET10N) to monitor the output pulse shape. We qualitatively monitor the pulse shape and level during operation with an oscilloscope to ensure its presence and that its shape has not unknowingly changed. The 95% leg is coupled into two electro-optic modulators (EOM; BATI Nanona) oriented in series and acting as Pockel cells with cross polarizers, each with 20 dB of “off” isolation, to further increase the isolation between the MO and the EDFA. The EOMs are driven with an identical square modulation signal to provide minimal isolation during the outgoing pulse and maximum isolation otherwise. The output of the EOMs is coupled to a manual optical attenuator to control the amount of average power provided

to the EDFA ($16 \mu\text{W}$ is required by the manufacturer). The attenuator output is connected to the head unit via a 10 m armored single-mode fiber to allow remote placement of the lidar head unit in environmentally challenging conditions.

Upon entry to the head unit, the armored fiber is coupled to the input of the EDFA where only the third-stage pump current of the EDFA is user tunable. A combination of the input pulse shape and pump current are selected to achieve a desired pulse width while maintaining eye safe operation and minimizing contamination of the atmospheric return from amplified, CW leak-through. In the laboratory, prior to deployment, the amplifier output is monitored during initial tuning of the input pulse shape and third-stage pump current to minimize Brillouin scattering in the final stage of the amplifier and output fiber caused by high intensity light. This Brillouin scattered light propagates in both directions and can cause damage to the first stage of the EDFA (Kobyakov et al. 2010; Ippen and Stolen 1972). These considerations typically limit the average launched power to $<1 \text{ W}$ for the most commonly used pulse lengths. As per Fig. 1, the input pulse shape to the EDFA leaving the AOM is non-Gaussian and is composed of a slow exponential rise followed by a steep linear decay; its shape is dictated by the time-dependent gain profile of the

amplifier so each desired pulse length requires a slightly different waveform to ensure a nearly Gaussian output shape at various EDFA pump currents. The output pulse shape from the EDFA is monitored with a transfer lens set (L2 in Fig. 1) and a 10-m, 550- μm -diameter, multimode fiber monitoring the off polarization path through the first polarizing beam cube (PBC; in Fig. 1) coupled to a detector (Thorlabs PDB430C-AC) at the base unit. The detector signal is measured with an oscilloscope and displayed to the user to ensure the pulse shape or level do not appreciably deviate from the original set points. The EDFA output fiber is a 20- μm -diameter core, multimode, PM, large mode area fiber with an $M^2 < 1.5$ and a pigtail length of 35 cm that is set from the manufacturer. The 35 cm pigtail is the driving factor that mandates the EDFA and free-space section (discussed below) be collocated in the head unit. Following the EDFA, the amplified pulse is coupled into the free-space optics of the T/R switch and telescope, see section 2b.

b. Free-space components

The optical head section of the lidar is composed of the EDFA, described above, a free-space T/R switch, and a folded Keplerian telescope. Linearly polarized light leaves the EDFA fiber output, is collimated (L4 in Fig. 1), and directed into a polarizing beam cube (1000:1 polarization isolation ratio; PBC in Fig. 1). The beam is then directed through the secondary of the telescope (L3), through a $\lambda/4$ plate located at the beam waist, thus imparting a circular polarization, into the objective lens (L1), and then into either a scanner or directly into the atmosphere. The lenses are chosen to create a telescope of magnification 16.7 that is nominally $f/8$ as a design balance between minimizing spherical aberrations and physical size. The telescope spatial footprint is additionally minimized by using turning mirrors TM1 and TM2 to fold the beam within the optical head. A Keplerian design was chosen to allow only one scattering optical component (L1) after the $\lambda/4$ plate while still allowing a mechanically robust design using off-the-shelf lenses and optomechanical lens tubes and cages. The larger spot size at the L1 optic reduces the sensitivity of the system due to back reflections. The single scattering optic reduces the possibility that the scattered light will couple back through the T/R switch and saturate the detector while the pulse is leaving the telescope. The telescope has an adjustable focus that is typically set at infinity though can be set closer if more sensitivity closer to the lidar is desirable, like in an aircraft where the ground limits the maximum measurable range. After the beam leaves the telescope and propagates through the atmosphere it will Mie scatter off of aerosols in the atmosphere with a small fraction returning directly to the

lidar. The returned light then passes through the $\lambda/4$ waveplate again imparting a combined $\lambda/2$ polarization shift that causes the light to pass through the polarizing beam cube rather than reflecting. The atmospheric return beam is adjusted with two cage mounted turning mirrors (TM3 and TM4) and passes through a beam expander, focal lengths of 40 mm (L5) and 50 mm (L6), to optimally couple onto a single mode fiber. Note that during lidar construction, the local oscillator (LO) beam is used as a source and is back propagated through the atmospheric return path to enable beam profiling and alignment. The return path is coupled from free space into a 9 μm fiber with a fiber collimator (L7). This light is sent back to the base unit using another, 9 μm , single-mode, PM, 10 m armored fiber to be mixed with the MO via a 50% fiber beam splitter and measured on a balanced detector (Thorlabs PDB 430C-AC). The backscattered atmospheric signal is measured with heterodyne detection; see section 2c. Free-space optics in the T/R switch allow both optimization of optical coupling and alignment and a high-intensity output beam that would cause Brillouin scattering in subsequent fiber-based components. The extensive use of optical fibers and solid-state optical components allows this system to have compact size and robust performance compared to earlier, free-space optics based Doppler lidars developed at NOAA (Grund et al. 2001; Brewer and Hardesty 1995; Post et al. 1982; Henderson et al. 1993; Koch et al. 2007). All free-space components are mounted with 30 mm cage mounts or lens tubes to increase rigidity and facilitate alignment. Additionally, all unspecified optical components, free-space and fiber, are off-the-shelf items sold from the major optics suppliers.

c. Data acquisition

The acquisition of the Doppler signal follows the schematic shown in Fig. 2. The heterodyne detector responds to the difference frequency between the atmospheric return and the LO. The difference frequency is centered at the IF (f in Fig. 2) imparted by the AOM and ranges over ± 31.0 MHz (± 25 m s $^{-1}$) due to the Doppler shift imparted by the component of atmospheric motion along the lidar line of sight (LOS).

The signal from the detector is sent through an RF blanking circuit that switches in a -40 dB attenuator into the data acquisition circuit while the optical pulse is leaving the telescope and provides an unattenuated path during collection of atmospheric returns; henceforth, we call this circuit the “RF blanking circuit.” This attenuator ensures that the electronic front end of the digitizer does not become saturated from the high detector output resulting from reflections of the outgoing pulse from the optical surfaces of the T/R switch and telescope.

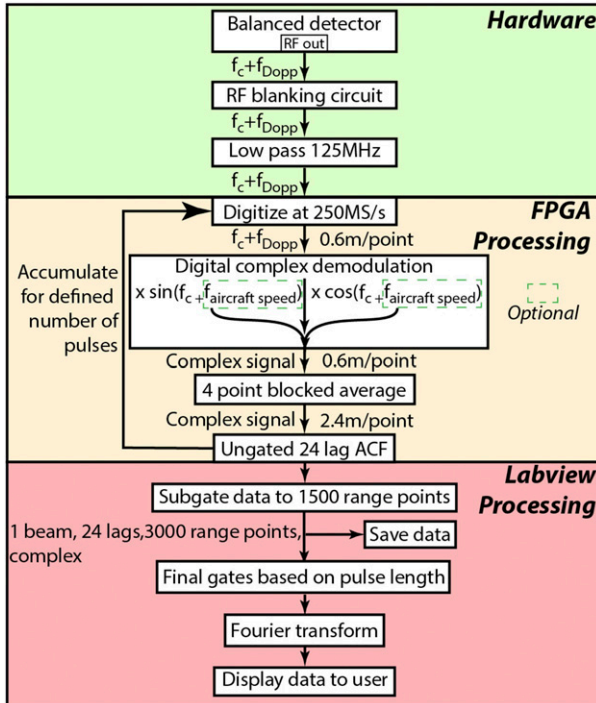


FIG. 2. Schematic of data flow and processing for MD2. ACF: autocorrelation function; FPGA: field programmable gate array; f_c : carrier frequency; f_{Dopp} : atmospheric Doppler frequency; $f_{aircraft\ speed}$: Doppler shift induced by the aircraft motion; ACF: autocorrelation function, RF: radio frequency, FPGA: field-programmable gate array.

Once the optical pulse leaves the telescope, the RF blanking circuit switches to allow the atmospheric return signal to pass unattenuated. Next, the detector signal is sent into a low-pass filter with a cutoff frequency at 125 MHz to prevent aliasing from higher frequencies and harmonics.

The filtered signal is digitized at 250 MS s^{-1} at 14 bits and fed to the field-programmable gate array (FPGA). The digitization frequency corresponds to a physical spacing of the return signal of 0.6 m per digitized point. If MD2 is being deployed in an aircraft, the aircraft speed and orientation, measured with an inertial navigation unit (INU; VectorNav VN-200), and azimuthal angle of the beam, are used to compute an effective Doppler frequency resulting from the motion of the aircraft. This resultant Doppler shift is then used to digitally shift the center of the bandpass filter to remove the effect of the aircraft motion from the Doppler wind signal typically contaminated with the aircraft motion. Without this step, the aircraft speed projected into the LOS of the measurement would shift the retrieved velocity (aircraft plus atmospheric Doppler) outside the $\pm 25\text{ m s}^{-1}$ ($\pm 31.25\text{ MHz}$) system bandwidth. Within the FPGA, the signal is digitally complex demodulated

using the IF of 62.5 MHz plus the computed line of sight platform motion, which generates complex representation of the signal shifted to base band. A four-point boxcar low-pass filter is applied to the 0.6 m per digitizer point spacing to filter out the sum frequency and select the difference frequency between the signal and the IF; this creates a 62.5 MHz ($\pm 31.25\text{ MHz}$) bandwidth complex signal with a spatial resolution of 2.4 m per digitizer point. A 24-lag autocorrelation function (ACF) is computed for each subgate and accumulated for a user-defined number of pulses. The number of accumulated pulses defines the beam rate (i.e., accumulating 10000 pulses occurring at a 20 kHz rate yields a 2 Hz beam rate) and how fast the data are displayed to the user, typically 1–10 Hz.

The temporally accumulated, ungated ACF from the FPGA is sent to the PC (PXIe-8840) via the PXIe chassis bus to be saved, gated, spectrally processed into moment data (peak height, peak location, and peak width), and displayed. The PC runs LabVIEW, which averages adjoining 2.4 m points down to 1500 4.8 m subgates to reduce computational load. Each complex ACF data point is composed of 24 lags for each of the 1500 subgates. The ACFs from the 1500 subgates are then averaged together in range into gates based on the optical pulse length for that configuration and the starting subgate is selected when the reflections off the optics from the pulse leaving the lidar no longer contaminate the closest atmospheric return. Typically, MD2 is run with a 62.4 m pulse length (400 ns), the center of the first gate located at approximately 160 m away from the lidar, and is able to measure a maximum of 120 subsequent 62.4 m gates ($13\text{ subgates} \times 4.8\text{ m per subgate}$) for a maximum range of 7200 m. The maximum range is set by the repetition rate of the laser, typically 20 kHz, and the speed of light in air. Figure 3 shows lag-0, total signal strength (signal plus noise), and has indicated the atmospheric component, hard target return, where the gates start, and their uniform spacing after that point. Note that the center of the output pulse is used to define the center of the first gate and time = 0. The subgated ACFs within each gray column are averaged together to obtain a gated ACF that is later used to calculate the velocity estimate or other spectral moments. The attenuation due to the blanking circuit, described earlier in this section, is clear prior to the gate start position. Note that every fifth subgate is shown with a marker for clarity in the figure in the red trace and a dashed line has been added to indicate the noise floor of the system.

The 24-lag, complex ACFs for each gate are zero padded to 128 points and Fourier transformed. Their peaks are estimated by fitting ± 2 points around the maximum value in a spectrum with a second-order

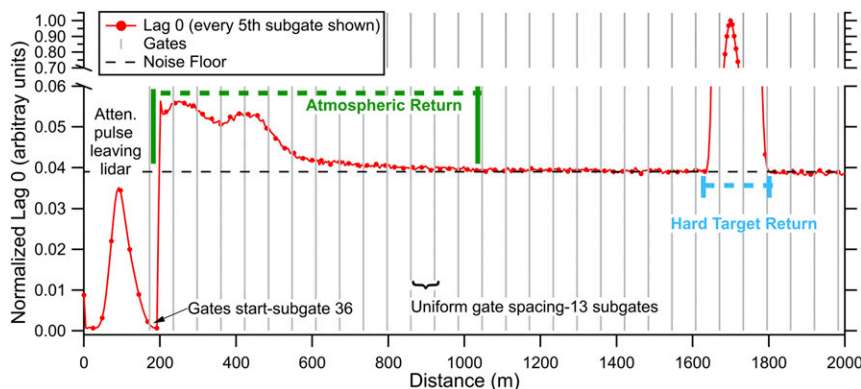


FIG. 3. Normalized lag-0 (signal plus noise) power-return example from an atmospheric/hard-target measurement example data in Boulder, Colorado. The atmospheric data are sectioned with a green dashed line with the hard-target return sectioned with blue. Gate widths are shown with gray vertical lines and are composed of 13 averaged subgates per gate. The magnitude of the hard-target return is shown with the split vertical axis relative to the weaker atmospheric return signal and the lidar noise floor is shown with a black dashed line. Atten.: attenuated.

polynomial and computing its maximum (Strauch et al. 1978). To investigate the difference in peak location estimate techniques, a Gaussian profile and a second-order polynomial were both fit to the peak of the same 128-point spectrum. The retrieved velocities for each profile did not deviate from each other by more than the Cramer–Rao lower bound (CRLB) (Rye and Hardesty 1993; Frehlich 1993) described further in section 2f. The CRLB yields the best possible precision for a measurement of a wind speed for a given lidar configuration (temporal and spatial resolution) and signal wideband signal-to-noise ratio (wbSNR). For this work, wbSNR is defined as the ratio of the signal area divided by the total noise area over the entire bandwidth. Since the difference of the two methods was less than this value, their difference was not determined to be significant. Therefore, the polynomial peak method was used for computational efficiency.

Approximately once every hour for 30 s, a shutter is thrown in front of the telescope and the signal is averaged. These data are used to estimate the spectral noise characteristics of the system. Because the dominant noise source, shot noise from the local oscillator, is white, these data can be used to quantify the differential electrical gain across the passband of the system. This differential gain manifests in the Doppler spectrum as <3 and <1 dB with and without the blanking circuit installed, respectively, of structure on the noise spectrum that competes with low signal levels from the atmosphere. Since a maximum value search algorithm is used to determine which peak in a spectrum to fit, any variation in the baseline combined with random noise peaks can create a maximum value larger than the actual Doppler peak. This peak can then be incorrectly selected and fit as

the Doppler signal instead of the actual Doppler peak. To combat this incorrect selection possibility, the noise ACF is subtracted from the signal ACF prior to taking the FFT and fitting the peak. This subtraction whitens the spectrum and removes the varying baseline structure. This extends the low wbSNR signal range from -25 to -28 dB thus increasing measurement range. The Doppler velocities are then computed for every gate and displayed to the user as functions of time, range, velocity, and magnitude.

The LabVIEW program affords the user access to every aspect of the electro-optical, data acquisition, and data processing parameters of the lidar. In addition to displaying the real-time lidar output, the LabVIEW program controls a scanner (section 2d), controls the arbitrary waveform card for the AOM, the on and off states of the EOMs, EDFA output power, system shutter, and the aircraft pitch compensation control loop, see section 3a.

d. Beam scanning

MD2 uses a vertically oriented wedge scanner to perform plan position indicator (PPI) scans in order to measure horizontal and vertical wind fields at each of the range gates through a velocity–azimuth display (VAD) technique (Browning and Wexler 1968). Currently, MD2 uses a single axis scanner with an optical grade silicon wedge that deflects the beam at 15° relative to the axis of the scanner. The scanner has been used on deployments where long-term environmental protection is not required, like on aircraft. It is typically run at no more than 60°s^{-1} to reduce beam sweeping contamination during the scan, i.e., averaging of wind fields over an azimuthal angle equal to the scanning speed/beam rate.

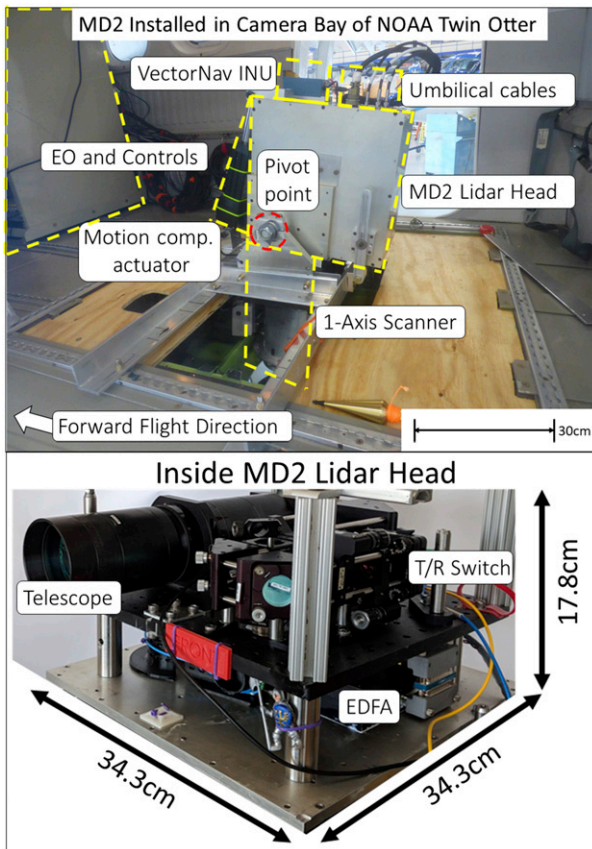


FIG. 4. MD2 as installed in the Twin Otter, shown here in the scanning configuration utilized for profiling horizontal wind fields. The electro-optics and control electronics are not shown for clarity but were mounted on server racks indicated with “EO and controls.” EO: electro-optics; INU: inertial navigation unit; comp.: compensation.

The scanner is driven by a stepper motor through a minimal backlash gear train with its position monitored by an encoder. The entire assembly is mounted to the lidar through a slip-fit XY (perpendicular to the beam propagation direction) adjustment stage and a tip-tilt adjustment plate. The XY and tip-tilt adjustments are required to ensure the rotation axis of the wedge is colligned to the propagation direction of the beam as it leaves the lidar. The scanner is aligned to the centerline of the aircraft in the field and is periodically checked to ensure there is no slippage of the encoder during operation. During aircraft deployments, the pitch angle of the scanner–lidar assembly can be dynamically changed using a linear actuator and a pivot point mount (“motion comp. actuator” in Fig. 4) to maintain pointing relative to Earth regardless of aircraft pitch. This articulation also enables the direct measurement of vertical winds under the aircraft by pitching the lidar 15° and rotating the wedge to the forward direction thereby counteracting the wedge

deviation and pointing the beam perpendicular to the ground. The actuator is capable of 22° of articulation in the aft (rearward) direction, 9° in the fore (forward) direction, with full articulation taking approximately 5 s. The pitch compensation control loop keeps the lidar to within 0.13° of the desired pointing angle relative to the ground under normal (straight and level) aircraft flight motion.

e. Mechanical and environmental considerations

The optics package (T/R switch and telescope) is mounted to a $30.5\text{ cm} \times 30.5\text{ cm} \times 1.3\text{ cm}$ aluminum optical breadboard with the EDFA mounted to a $34.3\text{ cm} \times 34.3\text{ cm} \times 0.96\text{ cm}$ aluminum plate creating a two-tiered setup, shown in Fig. 4. The breadboard is mounted to the aluminum plate via 7.6-cm-tall standoffs. With this design, the head unit is considered a semipermanent assembly that is easily incorporated into the various mounting schemes such as those described in sections 3a and 3b. Any future deployment configuration can therefore utilize MD2 so long as it can accommodate the $34.3\text{ cm} \times 34.3\text{ cm} \times 17.8\text{ cm}$ optical head assembly and be mounted within the 10 m reach of the umbilical cables from the base electronics 1/2 height rack.

For its first deployment, MD2 was mounted in the NOAA Twin Otter, a twin-engine turboprop aircraft operated by the NOAA Aircraft Operations Center. The aircraft is reconfigurable for various scientific experiments, is unpressurised, has the lowest operational cost, and is the smallest manned aircraft in the fleet. The Twin Otter’s “low and slow” flight paths are ideal for airborne lidar measurements because of the increased, along-track spatial resolution of the measurements. For reference, typical Twin Otter flight speeds are 120 kt ($1\text{ kt} \approx 0.51\text{ m s}^{-1}$) at less than 3000 m above sea level with the ability to increase the ceiling to 5400 m with supplemental oxygen. Mounting MD2 in the NOAA Twin Otter camera bay, section 3a, required a mechanically robust design that restricts any component separation during a 10 g impact. Therefore, the lidar was housed in a 0.96-cm-thick $34.3\text{ cm} \times 34.3\text{ cm} \times 20.3\text{ cm}$ aluminum box. The box was designed to provide a stiff mounting platform that does not transfer appreciable stresses to the optical breadboard or components inside the box. As seen in Fig. 4, the box mounts the axles (circled in red in the figure) and actuator (indicated in the figure) for lidar rotation and requisite support structure for mounting in the unpressurized Twin Otter bay. The lidar head is not sealed against the environment though aside from condensation issues associated with rapid altitude changes in a humid environment, this has not shown to be problematic in aircraft deployment.

The second deployment of MD2 was during the Propagation of Intraseasonal Tropical Oscillations

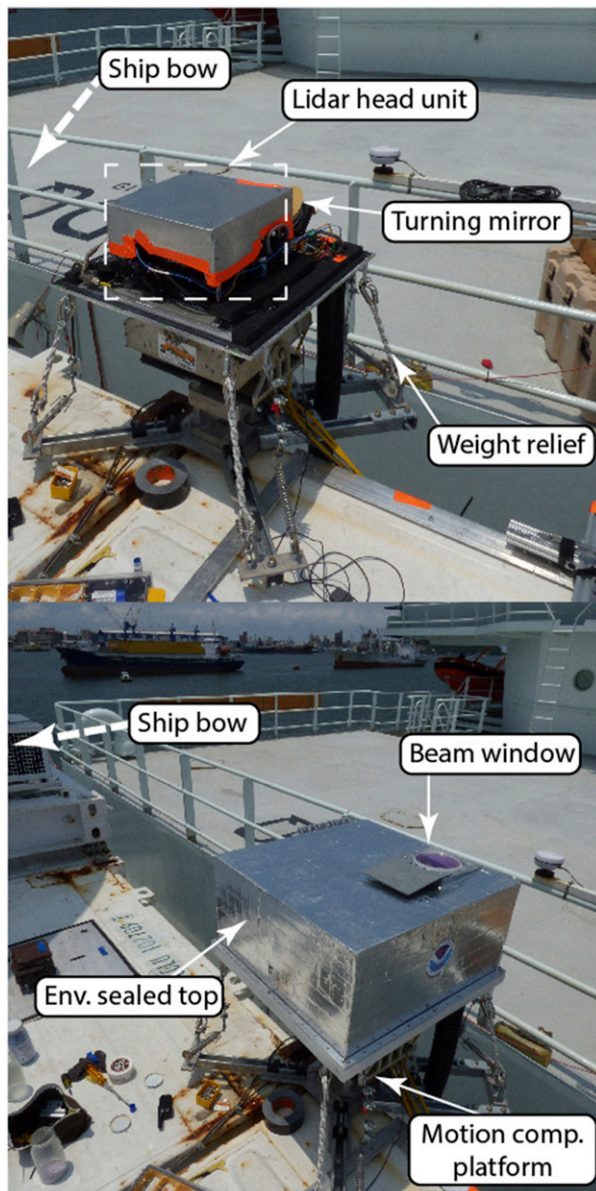


FIG. 5. (top) The MD2 assembly with the environmentally sealed top removed, mounted on the corner of a seatainer. (bottom) The assembly with the environmentally sealed top installed, covered with aluminum tape to reject incident solar radiation. “Weight relief” denotes bungee cords that help prevent the platform from freely tipping over when power was removed from the motion compensation platform motors. Inside the seatainer at the bottom of these pictures was housed the electronics and electro-optics that ran the lidar. Env.: environmentally; comp.: compensation.

(PISTON; described later in [section 3b](#)) campaign and required the optical head of MD2 to be sealed against sea spray and air. To seal the lidar unit, a 61 cm \times 61 cm \times 30 cm polyethylene tub, seen in [Fig. 5](#), was sealed with rubber weather stripping to a 60 cm \times 60 cm \times 0.64 cm aluminum plate. The polyethylene

tub was covered with aluminum tape to reject incident solar radiation. The heat rejection face of the EDFA was mounted through two aluminum plates and heat sink compound to the main plate of the motion compensation assembly to allow rejection of heat to the environment. The lidar head unit, two INUs, one for monitoring and one for motion control, desiccant, and a turning mirror were mounted on the plate within the tub. To allow for vertical operation, the lidar beam was turned perpendicular to the aluminum plate with a flat, elliptic, gold mirror. The beam passed through the protective tub via a 12.7-cm-diameter window AR coated for 1543 nm transmission. The fiber optic and electrical cables passed into the box via sealed bulkhead connectors and the cables were protected on the outside of the box by a flexible plastic corrugated conduit. The conduit was coupled to 3 in. PVC pipe that allowed direct access to the inside of the seatainer where the lidar control unit was housed. The sealing design, desiccant, and thermal considerations kept the lidar head unit to a continually operable temperature ($<65^{\circ}\text{C}$) and relative humidity ($<5\%$) for both 1-month legs (two total months) of the experiment in August through October in the Philippine Sea (approximately 12°N , 135°E). In this region, the average daytime temperature and relative humidity ranged from 25° to 29°C and 70% to 90%, respectively. During deployment, the lidar was mounted to a motion compensation platform to keep the beam pointing vertically while undergoing ship roll and pitch. The platform exhibited problems reading the INU signal and therefore problems controlling the pitch and roll. It could only maintain vertical pointing with a standard deviation in roll of 1.1° and 1.0° in pitch in waves with standard deviations of 1.3° in roll and 1.2° in pitch. Redesigns of this platform are currently being undertaken to enable pointing accuracy of $\pm 0.2^{\circ}$ over $\pm 30^{\circ}$ pitch and roll. The vertical motion of the ship was measured by an inertial navigation unit (VectorNav VN200 and Inertial Laboratories MRU) and removed from all subsequent lidar data. All critical operations, optical, electrical, and mechanical parameters of the lidar have been listed for clarity in [Table 1](#).

f. Instrument characterization

The precision of MD2, like all Doppler lidars, is theoretically bounded by the CRLB for the averaging of Gaussian random processes as applied to lidar measurements ([Rye and Hardesty 1993](#); [Frehlich 1993](#); [Porat and Friedlander 1986](#); [Rye 2000](#)). [Figure 6](#) shows the calculated CRLB computed via [Rye \(2000\)](#) for MD2 together with estimates of the random component of the noise (instrumental noise) calculated using a 5 h dataset of 2 Hz velocity measurements (36 000 samples) collected

TABLE 1. Listing of all major lidar parameters as deployed in this work, where D is depth, W is width, and H is height.

Key lidar parameters	
Wavelength	1.543 μm
Pulse rate	10–20 kHz
Pulse length	166–1000 ns
Beam rate	≤ 10 Hz
Beam diameter	75 mm
Average launched optical power	0.5–1 W
Maximum range in typical configuration	7200 m
Typical range resolution	33.6–62.4 m
Head mass on aircraft	68.1 kg
Head dimensions in aircraft ($D \times W \times H$)	34.3 cm \times 34.3 cm \times 17.8 cm
Head mass on ship	29.4 kg
Head dimensions on ship ($D \times W \times H$)	61.0 cm \times 61.0 cm \times 30.0 cm
Base mass	158.7 kg
Base dimensions ($D \times W \times H$)	58.4 cm \times 48.3 cm \times 121 cm
Wall power draw	300 W
Measured velocity bandwidth	± 25 m s $^{-1}$

staring horizontally in Boulder, Colorado. The velocity standard deviations are averaged into 1 dB wbSNR bins to generate the figure. The instrument velocity precision is calculated using two methods operating on the velocity time series: 1) a back extrapolated linear fit of the ACF for each range gate as described by [Lenschow et al. \(2000\)](#), and 2) using the tail of the power spectrum to estimate the total instrumental variance ([Hildebrand and Sekhon 1974](#)). In this data series, the zeroth lag of the ACF contains both instrument noise variance and atmospheric velocity variance. The instrument noise is white so it will be decorrelated by lag 1 leaving only the variance due to atmospheric turbulence. To account for any unresolved atmospheric variability that occurs at temporal scales smaller than one sample, lags 1–4 are then used to linearly back interpolate the amount of atmospheric variation measured in the zeroth lag ([Lenschow et al. 2000](#)). The difference between this value and the total zeroth-lag peak yields an estimate of the random, instrumental noise component for the measurement; results are shown in [Fig. 6](#). Hard-target and cloud returns were excluded from the velocity time series for the values calculated in [Fig. 6](#) since they can contaminate the noise estimate. [Figure 6](#) also shows uncertainty estimates for computing the standard deviation using the tail of the power spectral density for the time series. This computation assumes there is no atmospheric signal being measured in the high-frequency regime in the last 95% of the spectrum so all noise present is due to the instrument and not atmospheric sources. This technique does not allow for unresolved atmospheric variability in

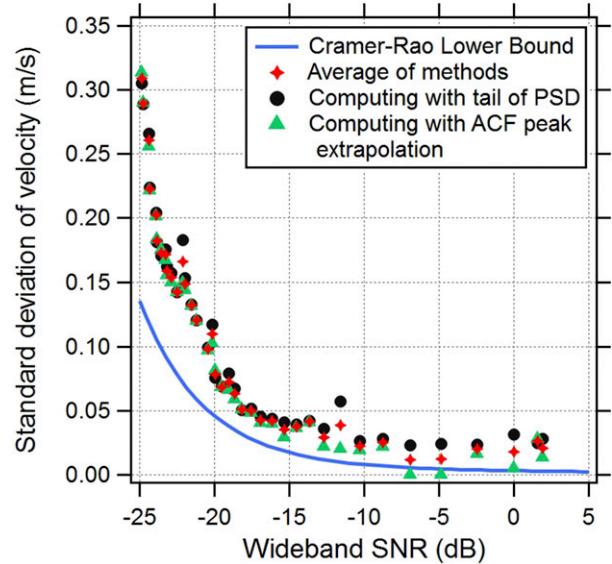


FIG. 6. A comparison of computed velocity standard deviations as a function of wbSNR of MD2 as compared to the ideal CRLB for data taken with a 2 Hz beam rate, 20 kHz pulse rate, and 400 ns pulse length. PSD: power spectral density; ACF: autocorrelation function.

the sub-single-time-step scale so it slightly overestimates the instrumental noise.

As shown in [Fig. 6](#), the velocity standard deviation of MD2 in high wbSNR regimes, > -17 dB, is approximately 2.5 cm s $^{-1}$, which is double the minimum possible value estimated using the CRLB calculations for this wavelength (1543 nm), pulse length (400 ns), beam rate (2 Hz), pulse repetition rate (20 kHz), and sampling frequency (62.5 MHz). The velocity standard deviations computed from the measurements increases as expected with decreasing wbSNR but follows the CRLB curve up to approximately -20 dB where they start to rapidly diverge from the calculation. Between -25 and -28 dB is where the returned velocities from MD2 are not typically completely continuous so their uncertainties have not been shown on this plot. At -30 dB, no reliable velocities are generally retrieved so the velocity standard deviation limits to ± 10 m s $^{-1}$. The few instances at high wbSNR where the filled green triangles drop below the CRLB are artifacts of the linear extrapolation process when a sharp discontinuity occurs in the ACF between lags 0 and 1 ([Lenschow et al. 2000](#)). The average of the two methods should be used to interpret the plot.

Velocity measurements as a function of optical output power and range were also investigated using measurements taken from our laboratory in Boulder, Colorado. MD2 collected 2 minutes of data at each of four pump currents (4, 5, 6, 7 amps) in a horizontally staring configuration with a 400 ns pulse (62.4 m gate

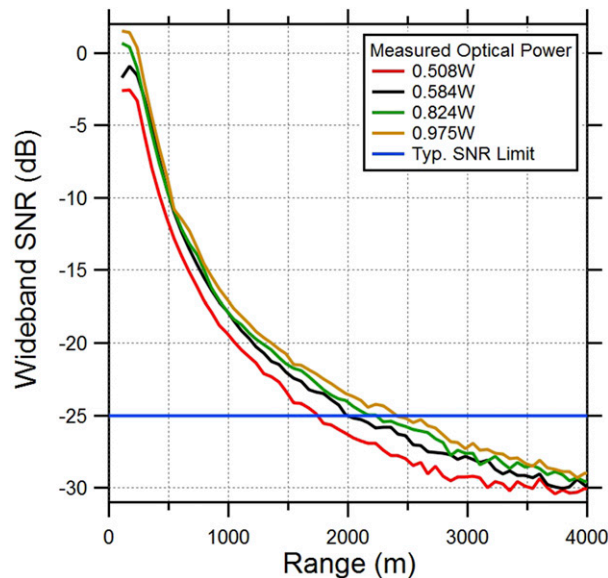


FIG. 7. Plot of wbSNR vs range for various levels of launched optical power. Increasing power output yields farther range, by approximately 500 m, but has a diminishing effect at approximately 0.8 W. We typically operate at 0.824 W, and the blue line at -25 dB is normally the low limit where velocity retrievals are considered reliable. The data here were collected with 2 Hz beam rates and 62.4 m gate lengths.

length). These pump current levels are typical for this instrument with 6 amps being the most commonly used setting. A collecting lens and a power meter (Thorlabs S302C) were attached to the output of the telescope and the launched power at each pump current setting was recorded. The launched power for the 4, 5, 6, and 7 amp settings were 0.508, 0.584, 0.824, and 0.975 W, respectively. The increase in resolved range using -25 dB as a common reference is clear in Fig. 7. By increasing the power from 0.508 to 0.975 W, maximum measurement range increases by about 500 m. New noise spectra were taken for each power level since the amount of leak through impacts the system noise characteristics and thus the Doppler return peak selection.

Systematic uncertainties for lidar velocity measurements are difficult to estimate due to the necessity of obtaining an air mass moving at a calibrated velocity some multikilometer distance away from the instrument. In lieu of a calibrated air mass, the typical method of calibration for this lidar is to ensure that stationary objects are measured as being stationary. Table 2 shows the two most commonly utilized pulse lengths for a singular EDFA pump current (6 amp), 200 and 400 ns, and the subsequent measured velocity of stationary buildings. Each measurement is the average of 400 velocity realizations and the uncertainty is the standard deviations of those values. A Haar wavelet analysis was

TABLE 2. Hard-target velocities (m s^{-1}) of the two most common pulse lengths at two different distances.

		Distance	
		1.5 km	5.8 km
Pulse length	400 ns	-0.18 ± 0.004	-0.17 ± 0.004
	200 ns	-0.12 ± 0.01	-0.10 ± 0.01

run on lag 0 of each beam to find the center of the peak of the return signal. A gate was created around that point and the ACFs within the gate were averaged and used to compute the velocity of the return signal. Though the values in the table vary slightly between ranges, the uncertainty in this hard target offset estimate is an order of magnitude less than the velocity uncertainty calculated for the high SNR regime presented in Fig. 6. Therefore, the variability in an atmospheric velocity measurement would dominate any difference in the hard target offsets. The values in the chart are used as offsets for the velocity of each gate width when measuring atmospheric returns. The hard target velocity offset is a result of the off-center frequency content generated during amplification in the EDFA that manifests as a Doppler shift. A hard target return illustrates how the entire backscattered pulse is measured by the system compared to a known, stationary velocity.

3. Experimental results

a. Wildfire studies in Florida

Wildfire studies in Florida, hereafter designated as Firewinds, was a campaign using MD2 to study wildfire wind dynamics of crop and controlled burns in Florida in the United States aboard the NOAA Twin Otter aircraft. The aircraft flights totaled 18.9 flight hours with the goal being to develop various scanning techniques, flight patterns, and investigate altitude effects on instrumentation over controlled burns. Firewinds was established in partial preparation for deployment to the experimental campaign, FIREX-AQ (ESRL 2019; <https://www.esrl.noaa.gov/csd/projects/firex/>), in 2019 where the instrument was deployed on a Twin Otter though with the goal of profiling the wind dynamics of larger, forest-burning wildfires occurring in the western United States. Measurements on this small aircraft were enabled by the compact format of MD2, shown in Fig. 4. The instrument took 2 days of initial setup and can now be ready to fly within a few hours.

Airborne Doppler lidars, while not new (Rothermel et al. 1998; Bilbro et al. 1984; Tratt et al. 2002; Li et al. 2010; Baidar et al. 2013; Tollerud et al. 2008; Kiemle et al. 2007), are underutilized in real-time wildfire research owing to the difficulty of deploying a flight-ready

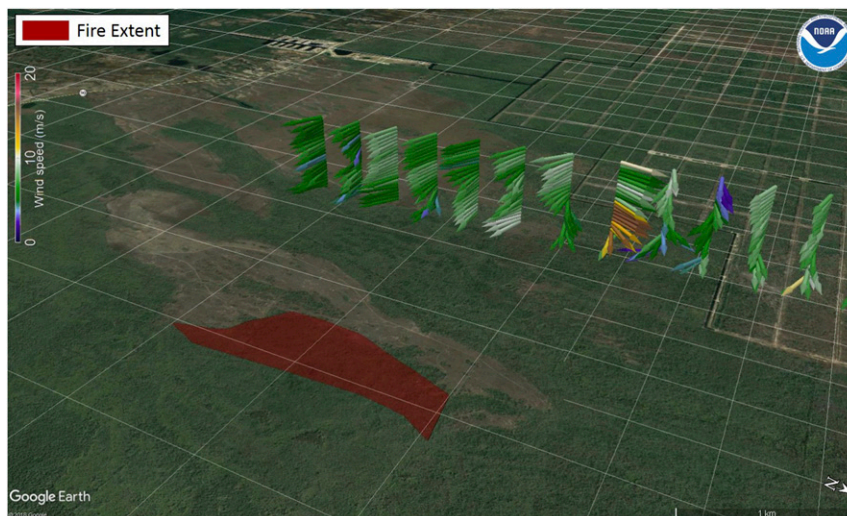


FIG. 8. Horizontal wind speed computed from the Twin Otter flights using VAD retrievals from continuous scanning of the beam at 60° s^{-1} . The arrow direction indicates wind direction for that specific height while color indicates speed. This flight was at an altitude of 1 km and the approximate fire location is also shown.

instrument and obtaining access to a burning fire front. Some work has been done with ground-based vehicles (Clements et al. 2007; Charland and Clements 2013) and fixed, ground-based systems (Banta et al. 1992) though these are limited by road access and changing fire direction. For Firewinds and future fire weather measurements, MD2 will provide valuable insight into fire dynamics and useful input data to wildfire models (Clark et al. 1996; Andrews et al. 2005; Finney 1995; Keane et al. 1998; Sharples 2008).

Both horizontal and vertical wind velocities are responsible for gas-phase fuel (volatile compounds pyrolyzed from the burning vegetation) transport and significant heat transfer of wildfires (Morvan and Dupuy 2004). Generally, there are two types of fires: plume and wind driven. A plume fire propagates via radiatively heating unburnt, upstream fuel causing secondary ignitions, whereas wind-driven fires propagate via fuel-gas recirculation and convective preheating of unburnt fuel, which causes secondary ignition. The fire investigated here was likely wind driven due to the moderate wind speeds, the limitation of the aerosol lofting to within the boundary layer, and the predictable movement of the fire.

All fires investigated in this work were burning when the aircraft arrived on station. The flights had two primary objectives:

- 1) Characterize the wind horizontal inflow of the fire on all accessible sides.
- 2) Characterize the vertical updraft velocities within the plume and over the fire front.

Future work with this lidar data will be to utilize it in computational wildfire models.

1) HORIZONTAL INFLOWS

Objective 1 was focused on profiling the horizontal inflows to a fire front. These wind fields are vital for understanding how incoming winds can drive fire propagation (Rothermel 1972). Not only do the horizontal winds provide fresh air to the burning fire front, they drive fire products and fuel gas downwind (Byram 1959; Sun et al. 2009; Kochanski et al. 2013).

Several controlled burns were investigated in the campaign with Figs. 8 and 9 showing example data from a single, well-profiled fire. The horizontal flows were characterized by scanning the lidar beam while flying approximately 1 km upwind of the fire front at an altitude of 1 km. A distance of 1 km upstream was chosen to ensure the lidar was measuring unperturbed effects of the horizontal inflow to the fire. The angle of the lidar relative to ground was measured and maintained with the control loop using the actuator shown in Fig. 4 (“motion comp. actuator”) and described in section 2d. Additionally, the frequency-shifting technique described in section 2c and Fig. 2 was employed, which removed the contribution of the aircraft speed to the measured LOS velocity.

In post processing, a VAD profile is fit to each completed scan to compute wind direction and speed at 33.6 m vertical resolution from 33.6 m above the ground to the aircraft or the top of the boundary layer, whichever comes first. It was assumed that the vertical velocity

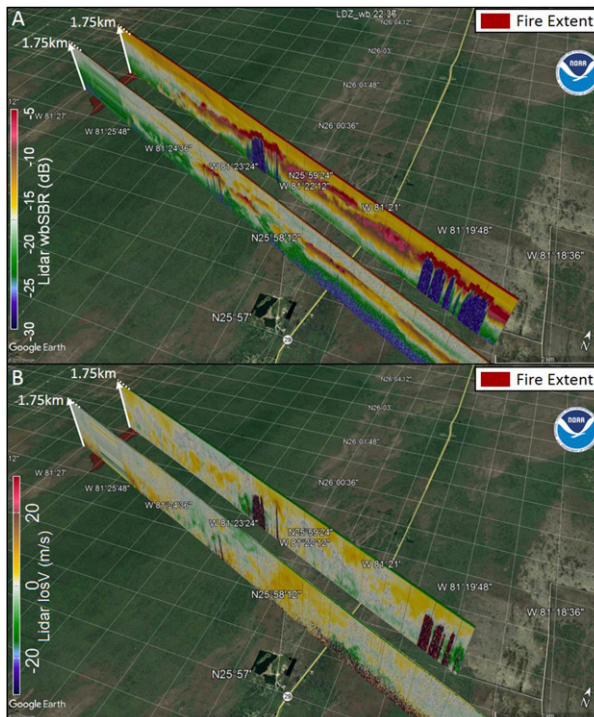


FIG. 9. (a) Vertical profile of aerosol distribution during a flight perpendicular to the fire front. It is clear that the aerosol enhancement is originating at the fire front and being lofted downwind of the fire. (b) As in (a), but for the computed vertical velocity over the fire. Updrafts are measured within the gasses leaving the fire front, and downdrafts are measured about 1.5 km downstream of the front. Transects are taken in the direction of mean transport.

at a given height was uniform over the course of a full scan though this is a known limitation to the VAD technique applied to steep elevation angle scans since nonuniform vertical velocities can be, depending on geometry and nonuniformity type, irretrievably mapped into horizontal velocity (Gasch et al. 2020). Figure 8 shows that a majority of the horizontal wind speeds were $<10 \text{ m s}^{-1}$ with uniform directionality feeding the fire. The vertical resolution of the measurements has been downsampled in the figure for clarity but was collected at a resolution of 33.6 m. The altitude variation in this area of Florida varied only approximately $\pm 5 \text{ m}$ over the investigated area so no influence of topology on horizontal flow dynamics was observed. Utilization of these data in fire models is ongoing and will be the subject of a future publication.

2) VERTICAL UPDRAFTS

Objective 2 was to profile the vertical winds and aerosol loading while flying perpendicular to the fire front to investigate the lofted altitude of fire products as well as the velocities of the vertical updrafts as the

buoyant gasses are transported downwind. To achieve a nadir orientation, the lidar was tilted 15° relative to Earth and the beam was rotated toward the front of the aircraft to direct the beam perpendicular to the ground. The 15° pitch of the lidar (perpendicularity of the beam to the ground) was maintained using the actuator control loop described above regardless of aircraft attitude.

The data in Fig. 9 were collected using a 10 Hz beam rate and 33.6 and 62.4 m range gates for the left and right traces, respectively, in each panel. The color scheme has been modified to be in the world view, i.e., warm colors are positive, away velocities as an observer on the ground would experience the winds. In Fig. 9a, the lofting of fire products is clear downwind from the fire front at approximately $26^\circ 00' \text{ N}$, $81^\circ 26' \text{ W}$ with the stable layer above the atmospheric boundary layer restricting the products from lofting higher than about 1750 m. This fire was burning in nonuniform patches of brush, which may contribute to why there is a difference in the aerosol return between the two traces. At no point did the fire have enough energy to push the products above the boundary layer like has been recorded during plume fires in dense forests (Fromm et al. 2000).

In Fig. 9, there are instances where the 33.6 m gates (the left plot in the two panels) cannot measure velocities near the ground, as shown by the blue color in Fig. 9a and the random colors in Fig. 9b. The lack of signal is a result of the 33.6 m gates averaging fewer photons for a single velocity realization, thus preventing measurement where a lower signal is present. While 33.6 m gates provide higher vertical resolution, their corresponding signal strengths are necessarily lower and require either higher aerosol loading or longer averaging times. The locations where there are no measured velocities below high wbsNR values (dark red) for both panels are instances where the aircraft flew over clouds that the lidar cannot penetrate.

Figure 9b shows retrieved vertical wind velocities for the traces in Fig. 9a. Clear updrafts (warm colors) appear directly after the fire front resulting from warm, buoyant fire products. As expected, the upward velocity decreases downwind as the gasses thermally equilibrate with the surrounding air. There are downdrafts downwind of the fire seen by the green colors in Fig. 9b under the enhanced aerosol layer. The source of the downdrafts are unknown but could be a result of circulation consistent with wind-driven fires.

b. PISTON

PISTON was a collaborative experiment designed to improve both model accuracy and physical understanding of the Madden-Julian oscillation (MJO) (Madden and Julian 1971) and the boreal summer intraseasonal oscillation (BSISO) (Yasunari 1980). Specifically, the portion of

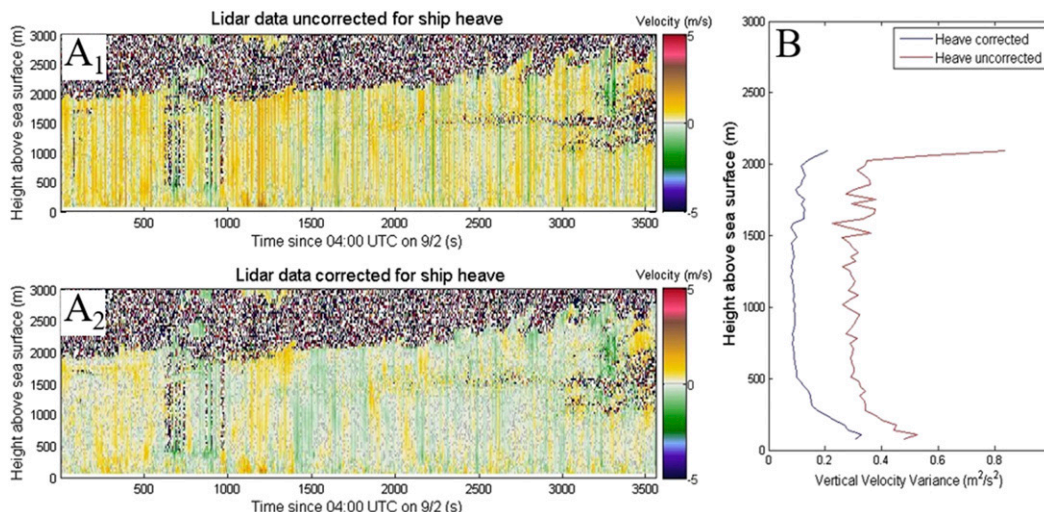


FIG. 10. [a(1)] Uncorrected velocity data where striping from the vertical motion of the ship is apparent. [a(2)] Removal of this heave after measurement by a VectorNav 200. (b) Vertical velocity variance as a function of height for both the corrected (blue) and uncorrected (red) data. The reduction in variance from removing heave is clear from the figure.

the experiment shown in this study set out to measure the effect the Maritime Continent has on the propagation of an MJO event. As part of this field campaign, MD2 performed continuous vertical stare measurements collocated with a vertically oriented, motion-stabilized W-band cloud radar (Moran et al. 2012). The goal was to form composite measurements of the vertical velocity variance, turbulence dissipation, and coherent plume height through the clear boundary layer and cloudy layers using MD2 and the W-band radar, respectively. See section 2e for a description of how MD2 was reconfigured for this ship-based deployment.

Measured vertical velocities for a 1 h time block are shown in Fig. 10a. Figure 10a(1) shows the raw vertical velocities as measured by the lidar while at sea on the ship. The stripes from the heave of the ship are clear and mask the underlying vertical velocity of the atmosphere.

Figure 10a(2) was created by subtracting the measured heave of the ship, measured using the VectorNav 200, from the lidar data in Fig. 10a(1). Underlying atmospheric dynamics are revealed after removal. However, there is some slight uncorrected striping that is due to the imperfect motion compensation platform projecting the horizontal winds into the vertical measurements on the order of 1° – 2° off vertical.

Figure 10b shows the significant reduction of vertical velocity variance between the heave corrected and uncorrected data despite the residual striping.

4. Summary

The recent development of a compact, flexible, and robust micropulse Doppler lidar at NOAA's Earth

System Research Laboratory has enabled easier and more rapid field deployments. The system follows a master oscillator power amplifier configuration with the power amplifier, telescope, and transmit/receive switch separated with a 10 m umbilical cable from the rest of the unit. This configuration enables just the head unit to be mounted in a variety of orientations and on various platforms, like in the bay of a small aircraft, that were previously inaccessible or difficult to access with other instruments. The measurement precision approaches its theoretical minimum at high signal-to-noise ratios despite its small size and its systematic bias is of order 10 cm s^{-1} based on multiple hard-target retrievals; though this bias is removed from all velocity measurements during use. An in-house developed scanner can attach to the lidar to make VAD measurements of horizontal winds.

To test the instrument in its new configuration, it was deployed in two recent field experiments. The first was an aircraft based measurement investigating horizontal and vertical winds associated with wildfires. The horizontal flows were characterized upwind of the fire front and the vertical velocities were profiled over the flame. Clear enhancements from the lofted aerosols were measured along with where the atmospheric boundary layer limited their upward propagation. Additionally, updrafts and downdrafts immediately downwind of the fire front associated with aerosol enhancements were resolved. The lidar continuously operated under the significant temperature swings, condensing humidity, and vibrations associated with the aircraft landing without sustaining damage.

The second deployment took place on the R/V *Thomas Thompson*, in the Philippine Sea during the PISTON campaign. The lidar was mounted on the corner of a seatainer and put into an environmentally sealed enclosure. It operated nearly continuously for 2 months and withstood high rain, winds, and heat conditions. Unlike many commercial systems, this lidar is capable of easily changing its pulse length and beam rate to adapt to experimental necessities. For example, on PISTON, the pulse length and beam rates were changed to match those of a collocated W-band radar. Vertical atmospheric dynamics were revealed that were masked by the ship heave once the heave was measured and removed in post processing of the velocity data. The vertical velocity variance of atmospheric motion showed a significant reduction after this heave removal.

Micro Doppler 2 represents a useful and deployable Doppler lidar advancement. It is small enough to be utilized on previously untenable platforms and still retains the accuracy and precision required for useful scientific measurements. Every important aspect of the instrument can be modified in the field so its ability to be tuned to changing field requirements further enhances its experimental adaptability.

Acknowledgments. This research was performed while the lead author held an NRC Research Associateship award at the National Oceanic and Atmospheric Administration (NOAA). The authors would like to acknowledge the NOAA Climate Project Office Climate Variability and Predictability program for funding of the PISTON mission. The authors would like to additionally acknowledge the support given by the Aircraft Operations Center personnel during the wildfire flights, specifically Robert Miletic, Peter Boissonneault, Rick de Triquet, Shanae Coker, William Carrier, and David Keith, and the crew of the R/V *Thomas Thompson*, Sergio Pezoa, Byron Blomquist, and Simon de Szoke during the ship-based measurements.

REFERENCES

- Abari, C. F., A. T. Pedersen, and J. Mann, 2014: An all-fiber image-reject homodyne coherent Doppler wind lidar. *Opt. Express*, **22**, 25 880–25 894, <https://doi.org/10.1364/OE.22.025880>.
- Andrews, P. L., C. D. Bevins, and R. C. Seli, 2005: BehavePlus fire modeling system, version 4.0: User's guide. USDA Forest Service Tech. Rep. RMRS-GTR-106WWW, 132 pp.
- Baidar, S., and Coauthors, 2013: Combining active and passive airborne remote sensing to quantify NO₂ and O_x production near Bakersfield, CA. *Br. J. Environ. Climate Change*, **3**, 566–586, <https://doi.org/10.9734/BJECC/2013/5740>.
- Banta, R. M., L. D. Olivier, E. T. Holloway, R. A. Kropfli, B. W. Bartram, R. E. Cupp, and M. J. Post, 1992: Smoke-column observations from two forest fires using Doppler lidar and Doppler radar. *J. Appl. Meteor.*, **31**, 1328–1349, [https://doi.org/10.1175/1520-0450\(1992\)031<1328:SCOTF>2.0.CO;2](https://doi.org/10.1175/1520-0450(1992)031<1328:SCOTF>2.0.CO;2).
- , R. K. Newsom, J. K. Lundquist, Y. L. Pichugina, R. L. Coulter, and L. Mahrt, 2002: Nocturnal low-level jet characteristics over Kansas during CASES-99. *Bound.-Layer Meteor.*, **105**, 221–252, <https://doi.org/10.1023/A:1019992330866>.
- Bilbro, J., G. Fichtl, D. Fitzjarrald, M. Krause, and R. Lee, 1984: Airborne Doppler lidar wind field measurements. *Bull. Amer. Meteor. Soc.*, **65**, 348–359, [https://doi.org/10.1175/1520-0477\(1984\)065<0348:ADLWFM>2.0.CO;2](https://doi.org/10.1175/1520-0477(1984)065<0348:ADLWFM>2.0.CO;2).
- Brewer, W. A., and R. M. Hardesty, 1995: Development of a dual-wavelength CO₂ mini-MOPA Doppler lidar. *Proc. Coherent Laser Radar Conf.*, Massachusetts, MA, Optical Society of America, 293–296.
- Browning, K. A., and R. Wexler, 1968: The determination of kinematic properties of a wind field using Doppler radar. *J. Appl. Meteor.*, **7**, 105–113, [https://doi.org/10.1175/1520-0450\(1968\)007<0105:TDOKPO>2.0.CO;2](https://doi.org/10.1175/1520-0450(1968)007<0105:TDOKPO>2.0.CO;2).
- Byram, G. M., 1959: Forest fire behavior. *Forest Fire Control and Use*, McGraw-Hill, 90–123.
- Charland, A. M., and C. B. Clements, 2013: Kinematic structure of a wildland fire plume observed by Doppler lidar. *J. Geophys. Res. Atmos.*, **118**, 3200–3212, <https://doi.org/10.1002/jgrd.50308>.
- Clark, T. L., M. A. Jenkins, J. Coen, and D. Packham, 1996: A coupled atmosphere fire model: Convective feedback on fire-line dynamics. *J. Appl. Meteor.*, **35**, 875–901, [https://doi.org/10.1175/1520-0450\(1996\)035<0875:ACAMCF>2.0.CO;2](https://doi.org/10.1175/1520-0450(1996)035<0875:ACAMCF>2.0.CO;2).
- Clements, C. B., and Coauthors, 2007: Observing the dynamics of wildland grass fires: FireFlux—A field validation experiment. *Bull. Amer. Meteor. Soc.*, **88**, 1369–1382, <https://doi.org/10.1175/BAMS-88-9-1369>.
- ESRL, 2019: FIREX 2015-2019. NOAA, <https://www.esrl.noaa.gov/csd/projects/firex/>.
- Finney, M. A., 1995: FARSITE: A fire area simulator for fire managers. The Biswell Symposium: Fire issues and solutions in urban interface and wildland ecosystems, USDA Forest Service Tech. Rep. PSW-GTR-158, 13 pp., http://www.fs.fed.us/psw/publications/documents/psw_gtr158/psw_gtr158_03_finney.pdf.
- Frehlich, R., 1993: Cramer-Rao bound for Gaussian random processes and applications to radar processing of atmospheric signals. *IEEE Trans. Geosci. Remote Sens.*, **31**, 1123–1131, <https://doi.org/10.1109/36.317450>.
- Fromm, M., and Coauthors, 2000: Observations of boreal forest fire smoke in the stratosphere by POAM III, SAGE II, and lidar in 1998. *Geophys. Res. Lett.*, **27**, 1407–1410, <https://doi.org/10.1029/1999GL011200>.
- Garratt, J. R., 1994: Review: The atmospheric boundary layer. *Earth-Sci. Rev.*, **37**, 89–134, [https://doi.org/10.1016/0012-8252\(94\)90026-4](https://doi.org/10.1016/0012-8252(94)90026-4).
- Gasch, P., A. Wieser, J. K. Lundquist, and N. Kalthoff, 2020: An LES-based airborne Doppler lidar simulator and its application to wind profiling in inhomogeneous flow conditions. *Atmos. Meas. Tech.*, **13**, 1609–1631, <https://doi.org/10.5194/amt-13-1609-2020>.
- Grund, C. J., R. M. Banta, J. L. George, J. N. Howell, M. J. Post, R. A. Richter, and A. M. Weickmann, 2001: High-resolution Doppler lidar for boundary layer and cloud research. *J. Atmos. Oceanic Technol.*, **18**, 376–393, [https://doi.org/10.1175/1520-0426\(2001\)018<0376:HRDLFB>2.0.CO;2](https://doi.org/10.1175/1520-0426(2001)018<0376:HRDLFB>2.0.CO;2).
- Hall, F. F., R. M. Huffaker, R. M. Hardesty, M. E. Jackson, T. R. Lawrence, M. J. Post, R. A. Richter, and B. F. Weber, 1984: Wind measurement accuracy of the NOAA pulsed infrared Doppler lidar. *Appl. Opt.*, **23**, 2503, <https://doi.org/10.1364/AO.23.002503>.
- Henderson, S. W., P. J. M. Suni, C. P. Hale, S. M. Hannon, J. R. Magee, D. L. Bruns, and E. H. Yuen, 1993: Coherent laser

- radar at 2 μm using solid-state lasers. *IEEE Trans. Geosci. Remote Sens.*, **31**, 4–15, <https://doi.org/10.1109/36.210439>.
- Hildebrand, P. H., and R. S. Sekhon, 1974: Objective determination of the noise level in Doppler spectra. *J. Appl. Meteor.*, **13**, 808–811, [https://doi.org/10.1175/1520-0450\(1974\)013<0808:ODOTNL>2.0.CO;2](https://doi.org/10.1175/1520-0450(1974)013<0808:ODOTNL>2.0.CO;2).
- Intrieri, J. M., A. J. Bedard, and R. M. Hardesty, 1989: Details of colliding thunderstorm outflows as observed by Doppler lidar. *J. Atmos. Sci.*, **47**, 1081–1099, [https://doi.org/10.1175/1520-0469\(1990\)047<1081:DOCTOA>2.0.CO;2](https://doi.org/10.1175/1520-0469(1990)047<1081:DOCTOA>2.0.CO;2).
- Ippen, E., and R. Stolen, 1972: Stimulated Brillouin scattering in optical fibers. *Appl. Phys. Lett.*, **21**, 539–541, <https://doi.org/10.1063/1.1654249>.
- Jia, M., and Coauthors, 2019: Long-lived high-frequency gravity waves in the atmospheric boundary layer: Observations and simulations. *Atmos. Chem. Phys.*, **19**, 15 431–15 446, <https://doi.org/10.5194/acp-19-15431-2019>.
- Keane, R. E., J. L. Garner, K. M. Schmidt, D. G. Long, J. P. Menakis, and M. A. Finney, 1998: Development of input data layers for the FARSITE fire growth model for the Selway-Bitterroot Wilderness Complex. USDA Forest Service Tech. Rep. RMRS-GTR-3, 66 pp.
- Kiemle, C., and Coauthors, 2007: Latent heat flux profiles from collocated airborne water vapor and wind lidars during IHOP_2002. *J. Atmos. Oceanic Technol.*, **24**, 627–639, <https://doi.org/10.1175/JTECH1997.1>.
- Kobyakov, A., M. Sauer, and D. Chowdhury, 2010: Stimulated Brillouin scattering in optical fibers. *Adv. Opt. Photonics*, **2**, 1–59, <https://doi.org/10.1364/AOP.2.000001>.
- Koch, G., J. Beyon, B. Barnes, M. Petros, J. Yu, F. Amzajerdian, M. Kavaya, and U. Singh, 2007: High-energy 2 μm Doppler lidar for wind measurements. *Opt. Eng.*, **46**, 116201, <https://doi.org/10.1117/1.2802584>.
- Kochanski, A., M. A. Jenkins, R. Sun, S. Krueger, S. Abedi, and J. Charney, 2013: The importance of low-level environmental vertical wind shear to wildfire propagation: Proof of concept. *J. Geophys. Res. Atmos.*, **118**, 8238–8252, <https://doi.org/10.1002/jgrd.50436>.
- Langley DeWitt, H., D. J. Coffman, K. J. Schulz, W. A. Brewer, T. S. Bates, and P. K. Quinn, 2013: Atmospheric aerosol properties over the equatorial Indian Ocean and the impact of the Madden-Julian oscillation. *J. Geophys. Res. Atmos.*, **118**, 5736–5749, <https://doi.org/10.1002/jgrd.50419>.
- Lareau, N. P., and C. B. Clements, 2015: Cold smoke: Smoke-induced density currents cause unexpected smoke transport near large wildfires. *Atmos. Chem. Phys.*, **15**, 11 513–11 520, <https://doi.org/10.5194/acp-15-11513-2015>.
- Lawrence, T. R., D. J. Wilson, C. E. Craven, I. P. Jones, R. M. Huffaker, and J. A. L. Thomson, 1972: A laser velocimeter for remote wind sensing. *Rev. Sci. Instrum.*, **43**, 512–518, <https://doi.org/10.1063/1.1685674>.
- Lenschow, D. H., V. Wulfmeyer, and C. Senff, 2000: Measuring second- through fourth-order moments in noisy data. *J. Atmos. Oceanic Technol.*, **17**, 1330–1347, [https://doi.org/10.1175/1520-0426\(2000\)017<1330:MSTFOM>2.0.CO;2](https://doi.org/10.1175/1520-0426(2000)017<1330:MSTFOM>2.0.CO;2).
- Li, Z., C. Lemmerz, U. Paffrath, O. Reitebuch, and B. Witschas, 2010: Airborne Doppler lidar investigation of sea surface reflectance at a 355-nm ultraviolet wavelength. *J. Atmos. Oceanic Technol.*, **27**, 693–704, <https://doi.org/10.1175/2009JTECHA1302.1>.
- Madden, R. A., and P. R. Julian, 1971: Detection of a 40–50 day oscillation in the zonal wind in the tropical Pacific. *J. Atmos. Sci.*, **28**, 702–708, [https://doi.org/10.1175/1520-0469\(1971\)028<0702:DOADOI>2.0.CO;2](https://doi.org/10.1175/1520-0469(1971)028<0702:DOADOI>2.0.CO;2).
- Moran, K., S. Pezoa, C. Fairall, C. Williams, T. Ayers, A. Brewer, S. P. de Szoeke, and V. Ghate, 2012: A motion-stabilized W-band radar for shipboard observations of marine boundary-layer clouds. *Bound.-Layer Meteor.*, **143**, 3–24, <https://doi.org/10.1007/s10546-011-9674-5>.
- Morvan, D., and J. L. Dupuy, 2004: Modeling the propagation of a wildfire through a Mediterranean shrub using a multiphase formulation. *Combust. Flame*, **138**, 199–210, <https://doi.org/10.1016/j.combustflame.2004.05.001>.
- Pearson, G., F. Davies, and C. Collier, 2009: An analysis of the performance of the UFAM pulsed Doppler lidar for observing the boundary layer. *J. Atmos. Oceanic Technol.*, **26**, 240–250, <https://doi.org/10.1175/2008JTECHA1128.1>.
- Porat, B., and B. Friedlander, 1986: Computation of the exact information matrix of Gaussian time series with stationary random components. *IEEE Trans. Acoust. Speech Signal Process.*, **34**, 118–130, <https://doi.org/10.1109/TASSP.1986.1164786>.
- Post, M. J., R. A. Richter, R. M. Hardesty, T. R. Lawrence, and F. F. Hall, 1982: National Oceanic and Atmospheric Administration's (NOAA) pulsed, coherent, infrared Doppler LIDAR-characteristics and data. *Physics and Technology of Coherent Infrared Radar I*, Vol. 300, International Society for Optics and Photonics, 60–66.
- Rothermel, J., and Coauthors, 1998: Remote sensing of multi-level wind fields with high-energy airborne scanning coherent Doppler lidar. *Opt. Express*, **2**, 40–50, <https://doi.org/10.1364/OE.2.000040>.
- Rothermel, R. C., 1972: A mathematical model for predicting fire spread in wildland fuels. USDA Forest Service Res. Paper INT-115, 48 pp., https://www.fs.fed.us/rm/pubs_int/int_rp115.pdf.
- Rye, B. J., 2000: Estimate optimization parameters for incoherent backscatter heterodyne lidar including unknown return signal bandwidth. *Appl. Opt.*, **39**, 6086–6096, <https://doi.org/10.1364/AO.39.006086>.
- , and R. Hardesty, 1993: Discrete spectral peak estimation in incoherent backscatter heterodyne lidar. I. Spectral accumulation and the Cramer-Rao lower bound. *IEEE Trans. Geosci. Remote Sens.*, **31**, 16–27, <https://doi.org/10.1109/36.210440>.
- Senff, C. J., R. J. Alvarez, R. M. Hardesty, R. M. Banta, and A. O. Langford, 2010: Airborne lidar measurements of ozone flux downwind of Houston and Dallas. *J. Geophys. Res.*, **115**, D20307, <https://doi.org/10.1029/2009JD013689>.
- Sharples, J. J., 2008: Review of formal methodologies for wind-slope correction of wildfire rate of spread. *Int. J. Wildland Fire*, **17**, 179–193, <https://doi.org/10.1071/WF06156>.
- Stensrud, D. J., 1996: Importance of low-level jets to climate: A review. *J. Climate*, **9**, 1698–1711, [https://doi.org/10.1175/1520-0442\(1996\)009<1698:IOLLJT>2.0.CO;2](https://doi.org/10.1175/1520-0442(1996)009<1698:IOLLJT>2.0.CO;2).
- Strauch, R. G., R. A. Kropfli, W. B. Sweezy, W. R. Moninger, and R. W. Lee, 1978: Improved Doppler velocity estimates by the poly-pulse-pair method. *18th Conf. on Radar Meteorology*, Boston, MA, Amer. Meteor. Soc. 376–380, <http://adsabs.harvard.edu/abs/1978ame.conf.376S>.
- Strawbridge, K. B., and B. J. Snyder, 2004: Daytime and nighttime aircraft lidar measurements showing evidence of particulate matter transport into the northeastern valleys of the Lower Fraser Valley, BC. *Atmos. Environ.*, **38**, 5873–5886, <https://doi.org/10.1016/j.atmosenv.2003.10.036>.
- Sun, R., S. K. Krueger, M. A. Jenkins, M. A. Zulauf, and J. J. Charney, 2009: The importance of fire-atmosphere coupling and boundary-layer turbulence to wildfire spread. *Int. J. Wildland Fire*, **18**, 50–60, <https://doi.org/10.1071/WF07072>.

- Tollerud, E. I., and Coauthors, 2008: Mesoscale moisture transport by the low-level jet during the IHOP field experiment. *Mon. Wea. Rev.*, **136**, 3781–3795, <https://doi.org/10.1175/2008MWR2421.1>.
- Tratt, D. M., R. T. Menzies, M. P. Chiao, D. R. Cutten, J. Rothermel, R. M. Hardesty, J. N. Howell, and S. L. Durden, 2002: Airborne Doppler lidar investigation of the wind-modulated sea-surface angular retroreflectance signature. *Appl. Opt.*, **41**, 6941–6949, <https://doi.org/10.1364/AO.41.006941>.
- Tucker, S. C., C. J. Senff, A. M. Weickmann, W. A. Brewer, R. M. Banta, S. P. Sandberg, D. C. Law, and R. M. Hardesty, 2009: Doppler lidar estimation of mixing height using turbulence, shear, and aerosol profiles. *J. Atmos. Oceanic Technol.*, **26**, 673–688, <https://doi.org/10.1175/2008JTECHA1157.1>.
- Wächter, M., A. Rettenmeier, M. Kühn, and J. Peinke, 2008: Wind velocity measurements using a pulsed lidar system: First results. *IOP Conf. Ser.: Earth Environ. Sci.*, **1**, 012066, <https://doi.org/10.1088/1755-1315/1/1/012066>.
- Wang, C., H. Xia, M. Shangguan, Y. Wu, L. Wang, L. Zhao, J. Qiu, and R. Zhang, 2017: 1.5 μm polarization coherent lidar incorporating time-division multiplexing. *Opt. Express*, **25**, 20 663–20 674, <https://doi.org/10.1364/OE.25.020663>.
- , and Coauthors, 2019a: Relationship analysis of $\text{PM}_{2.5}$ and boundary layer height using an aerosol and turbulence detection lidar. *Atmos. Meas. Tech.*, **12**, 3303–3315, <https://doi.org/10.5194/amt-12-3303-2019>.
- , H. Xia, Y. Wu, J. Dong, T. Wei, L. Wang, and X. Dou, 2019b: Meter-scale spatial-resolution-coherent Doppler wind lidar based on Golay coding. *Opt. Lett.*, **44**, 311–314, <https://doi.org/10.1364/OL.44.000311>.
- Xia, Y., and Coauthors, 2017: Development of a solid-state sodium Doppler lidar using an all-fiber-coupled injection seeding unit for simultaneous temperature and wind measurements in the mesopause region. *Opt. Express*, **25**, 5264, <https://doi.org/10.1364/OE.25.005264>.
- Yan, Z., X. Hu, W. Guo, S. Guo, Y. Cheng, J. Gong, and J. Yue, 2017: Development of a mobile Doppler lidar system for wind and temperature measurements at 30–70 km. *J. Quant. Spectrosc. Radiat. Transfer*, **188**, 52–59, <https://doi.org/10.1016/j.jqsrt.2016.04.024>.
- Yasunari, T., 1980: A quasi-stationary appearance of 30 to 40 day period in the cloudiness fluctuations during the summer monsoon over India. *J. Meteor. Soc. Japan*, **58**, 225–229, https://doi.org/10.2151/JMSJ1965.58.3_225.